SCIENCE CHINA
Technological Sciences

• Article •

October 2023 Vol. 66 No. 10: 2882–2896
https://doi.org/10.1007/s11431-022-2436-y

A practical PID variable stiffness control and its enhancement for compliant force-tracking interactions with unknown environments

ZHANG Xin[1,2,3], ZHOU Hao[1,2,3], LIU JinGuo[1,2,3*], JU ZhaoJie[1,2,3,4], LENG YuQuan[5] & YANG ChenGuang[6]

[1] *State Key Laboratory of Robotics, Shenyang Institute of Automation, Chinese Academy of Sciences, Shenyang 110016, China;*
[2] *Institutes for Robotics and Intelligent Manufacturing, Chinese Academy of Sciences, Shenyang 110169, China;*
[3] *University of Chinese Academy of Sciences, Beijing 100049, China;*
[4] *School of Computing, University of Portsmouth, Portsmouth PO1 3HE, UK;*
[5] *Shenzhen Key Laboratory of Biomimetic Robotics and Intelligent Systems, Department of Mechanical and Energy Engineering, Southern University of Science and Technology, Shenzhen 518055, China;*
[6] *Key Laboratory of Autonomous Systems and Networked Control, College of Automation Science and Engineering, South China University of Technology, Guangzhou 510640, China*

Received December 20, 2022; accepted May 19, 2023; published online August 31, 2023

Compliant interaction control is a key technology for robots performing contact-rich manipulation tasks. The design of the compliant controller needs to consider the robot hardware because complex control algorithms may not be compatible with the hardware performance, especially for some industrial robots with low bandwidth sensors. This paper focuses on effective and easy-to-use compliant control algorithms for position/velocity-controlled robots. Inspired by human arm stiffness adaptation behavior, a novel variable target stiffness (NVTS) admittance control strategy is proposed for adaptive force tracking, in which a proportional integral derivative (PID) variable stiffness law is designed to update the stiffness coefficient of the admittance function by the force and position feedback. Meanwhile, its stability and force-tracking capability are theoretically proven. In addition, an impact compensator (Impc) is integrated into the NVTS controller to enhance its disturbance-suppression capability when the robot is subjected to strong vibration disturbances in complicated surface polishing tasks. The proposed controllers are validated through four groups of experimental tests using different robots and the corresponding results demonstrate that they have high-accuracy tracking capability and strong adaptability in unknown environments.

compliant interaction control, force tracking, PID variable stiffness, impact compensator, unknown environments

Citation: Zhang X, Zhou H, Liu J G, et al. A practical PID variable stiffness control and its enhancement for compliant force-tracking interactions with unknown environments. Sci China Tech Sci, 2023, 66: 2882–2896, https://doi.org/10.1007/s11431-022-2436-y

1 Introduction

Compliant interaction control plays an important role in modern manufacturing industries [1]. For instance, maintaining steady contact force is critical for improving the polishing quality of workpieces in robotic polishing and grinding tasks (Figure 1 [2]). Compliant control has been a hot topic in contact-rich manipulation scenarios [3]. From the current literature, researchers have proposed various compliant control algorithms, which can be mainly classified into direct and indirect force control strategies [4].

For direct force control, the interaction force and the joint torque are controlled by the force Jacobian matrix in an explicit closure of the force feedback loop [5]. When all the degrees of freedom (DoFs) of the end-effector are constrained, the robot-environment interaction becomes a complete force

*Corresponding author (email: liujinguo@sia.cn)

control problem. However, in most cases, the end-effector motion is partially constrained by the environment, and the unconstrained direction outputs a certain degree of interaction force. The hybrid force/position control [6] and the parallel force/position control [7] are the two most representative direct force control methods. The hybrid force/position control decomposes the endpoint motion and force of the operational space into two complementary orthogonal subspaces, and the endpoint motion and force are simultaneously controlled in these two decoupled subspaces [6]. In addition, knowledge of the environment model is a prerequisite in the hybrid force/position control framework [8]. In contrast, the parallel force/position control superimposes two controllers through a priority strategy, namely, the force controller is usually designed to prevail over the position controller when they are in dispute [7]. However, to achieve the desired compliant behavior, coordinating two controllers is difficult in the parallel force/position control framework.

Indirect force control aims to achieve the desired dynamic interaction behavior by dynamically regulating the relationship between the end-effector motion and the contact force. The well-known impedance control proposed by Hogan [9] is the fundamental method for indirect force control that regulates the interaction force by the target impedance function. There are two ways to implement the target impedance or admittance function (a virtual mass-spring-damper model) [10], namely, torque-based impedance control and position-based impedance control [11]. To avoid ambiguity, torque-based impedance control is termed impedance control, and the other is called admittance control. For impedance controllers, the target impedance function is implemented in the torque-controlled loop of the robot system, namely, in the dynamics control level. For admittance controllers, its target admittance function is implemented in the position/velocity-controlled loop of the robot system, namely, in the kinematics control level. In general, impedance controllers are suitable for systems with high bandwidth, but admittance controllers are appropriate for systems with low bandwidth [12]. As both controllers distinctly differ in their output characteristics and have complementary advantages and disadvantages, Ott et al. [10] proposed a hybrid control framework by switching between impedance and admittance controllers for a torque-controlled robot. Although impedance and admittance controllers are widely used, the classical impedance or admittance controller with fixed parameters can hardly regulate the interaction force to a desired value [13].

Figure 1 (Color online) Typical robotic polishing and grinding tasks [2].

Various control techniques have been proposed to achieve force tracking, which can be divided into two categories [14]: (1) real-time modification of the reference trajectory and (2) online adjustment of target impedance/admittance parameters. For the first category of methods, Jung et al. [15] proposed an environmental stiffness estimation technique to modify the reference trajectory and used a robust model-free controller to ensure the desired interaction force, where the model-free control adopts the time-delay estimation technique [16]. Lee and Wang [17] estimated the environment stiffness by the gradient method and the Lyapunov approach. Roveda et al. [18] used an extended Kalman filter to estimate the environmental stiffness. For the second class of methods, Seraji [19] proposed two adaptive admittance-based compliant control strategies in which proportional integral derivative (PID) and PI force compensators were designed for tracking the desired contact force. Lee and Buss [20] proposed an admittance controller with an online variable target stiffness coefficient to adjust the interaction force. Duan et al. [14] proposed a modified admittance controller with a variable damping coefficient to achieve the force-tracking interaction. Roveda et al. [21] proposed a force-tracking algorithm that combines a variable damping impedance controller and an adaptive saturation PI force controller to avoid overshooting. Balatti et al. [22] proposed a self-impedance tuning method by exploring the interaction relationship between the robot and the environment. Ferraguti et al. [23] proposed an energy-tank method to regulate the stiffness coefficient and achieve passive compliance behavior. Ding et al. [24] proposed an admittance controller based on virtual decomposition control to deal with manipulators with joint flexibility. Peng et al. [25] proposed a force sensorless admittance controller with neural learning to deal with unknown environ-

ments. He et al. [26] proposed a neural network controller to achieve adaptive admittance control. Li and Ge [27] proposed an iterative impedance learning method to obtain the desired impedance model. Hamedani et al. [28] proposed an intelligent impedance controller based on the wavelet neural network to realize adaptive force tracking in unknown environments. He and Dong [29] proposed an adaptive impedance learning method by the fuzzy neural network to optimize the target impedance parameters. Roveda et al. [30] proposed a sensorless optimal switching impact/force controller to deal with different operative situations in which the fuzzy logic theory is used to classify the task phase.

In addition, exploring human intelligence and transferring human knowledge [31] to design the controller is a hot trend. Ajoudani et al. [32] proposed the teleimpedance concept, which transfers the human arm stiffness information to the manipulator for achieving human-like compliant performance. Yang et al. [33] proposed a biomimetic impedance learning controller that imitates the regulation strategy of the human central nervous system to control robots with intelligent adaptability in unstable scenarios. Some imitation-learning-based methods employ dynamic movement primitives [34] and Gaussian mixture models [35] to learn the human variable stiffness behavior in some specific interaction tasks.

However, for designing a controller, one should consider robotic systems themselves. In practice, most robots are position/velocity-controlled robots only equipped with position and velocity interfaces in their application programming interfaces. Only a few companies provided joint torque or motor current interfaces to clients. In particular, some industrial robots are equipped with low-bandwidth sensors, so complex control algorithms may not be suitable. This paper focuses on practical compliant control algorithms for this kind of robots. Humans can intelligently regulate the interaction force by making their arms' muscles stiff or soft, where their arm stiffness adaptation is the key factor. Inspired by this behavior, we propose a novel variable target stiffness (NVTS) control strategy to achieve adaptive force tracking. The main contributions of this paper are concluded as follows.

(1) Inspired by the human arm stiffness adaptation behavior, an effective PID stiffness adaptation law is designed to update the target stiffness coefficient of our admittance controller for high-accuracy force tracking. Unlike other methods [21,30] that use PID as low-level controllers, we use it as an adaptive stiffness regulator.

(2) As an enhancement, an impact compensator (Impc) is integrated into the NVTS controller to increase its disturbance-suppression ability.

(3) The stability and force-tracking capability of the proposed methods are proven theoretically and various experimental tests are conducted to verify their strong practicability.

2 Preliminary knowledge

In this section, some preliminary knowledge of the robot-environment interaction, the environment model, and the admittance control are introduced. Then, we review two typical force-tracking strategies suggested by Jung et al. [15] and Lee and Buss [20], respectively.

2.1 Robot-environment interaction

For a 6-DoF robotic manipulator, its kinematics model in the velocity level is expressed as

$$\dot{\boldsymbol{x}} = \boldsymbol{J}(\boldsymbol{q})\,\dot{\boldsymbol{q}}, \tag{1}$$

where $\boldsymbol{q} \in \mathbb{R}^6$ is the joint space coordinate vector; $\boldsymbol{x} = \left[\boldsymbol{x}_p^{\mathrm{T}}, \boldsymbol{x}_r^{\mathrm{T}}\right]^{\mathrm{T}} \in \mathbb{R}^6$ is the Cartesian coordinate vector of the end-effector; $\boldsymbol{x}_p \in \mathbb{R}^3$ and $\boldsymbol{x}_r \in \mathbb{R}^3$ are related to the translational and rotational DoFs, respectively [30]; and $\boldsymbol{J}(\boldsymbol{q}) \in \mathbb{R}^{6\times 6}$ is the Jacobian matrix of the manipulator.

When the manipulator interacts with the environment, there exists an external generalized force $\boldsymbol{F}_e = \left[\boldsymbol{F}_p^{\mathrm{T}}, \boldsymbol{F}_r^{\mathrm{T}}\right]^{\mathrm{T}} \in \mathbb{R}^6$ acting on the endpoint, where $\boldsymbol{F}_p \in \mathbb{R}^3$ and $\boldsymbol{F}_r \in \mathbb{R}^3$ are the external force and torque vectors related to the Cartesian translation and rotation, respectively. For the one-dimensional translation case (Figure 2), $-F_p$ is the active force of the manipulator in the opposite direction of x_p^{ref}; x_p^e represents the environment position; x_p^c represents the compliant endpoint position; and x_p^d represents the desired endpoint position. The general dynamics model in joint space

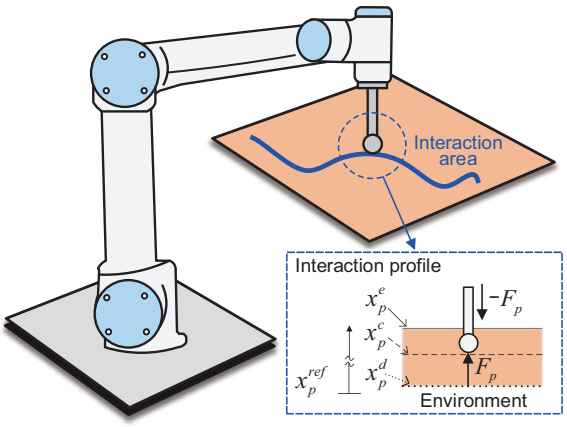

Figure 2 (Color online) Diagram of robot-environment translation interaction.

[3] is expressed as

$$\boldsymbol{H}(\boldsymbol{q})\ddot{\boldsymbol{q}} + \boldsymbol{C}(\boldsymbol{q},\dot{\boldsymbol{q}})\dot{\boldsymbol{q}} + \boldsymbol{g}(\boldsymbol{q}) = \boldsymbol{\tau} + \boldsymbol{\tau}_e, \tag{2}$$

where $\boldsymbol{H}(\boldsymbol{q}) \in \mathbb{R}^{6\times6}$ is the inertia matrix; $\boldsymbol{C}(\boldsymbol{q},\dot{\boldsymbol{q}}) \in \mathbb{R}^{6\times6}$ is the Coriolis and centrifugal matrix; $\boldsymbol{g}(\boldsymbol{q}) \in \mathbb{R}^6$ is the gravity force term; $\boldsymbol{\tau} \in \mathbb{R}^6$ is the joint driving torque term; and $\boldsymbol{\tau}_e = \boldsymbol{J}(\boldsymbol{q})^{\mathrm{T}}\boldsymbol{F}_e \in \mathbb{R}^6$ is the external torque term acting in the joint space.

The dynamics model in the Cartesian space [36] can be written as

$$\boldsymbol{\Lambda}(\boldsymbol{x})\ddot{\boldsymbol{x}} + \boldsymbol{D}(\boldsymbol{x},\dot{\boldsymbol{x}})\dot{\boldsymbol{x}} + \boldsymbol{F}_g(\boldsymbol{x}) = \boldsymbol{F}_\tau + \boldsymbol{F}_e, \tag{3}$$

where

$$\begin{aligned}
&\ddot{\boldsymbol{x}} = \boldsymbol{J}(\boldsymbol{q})\ddot{\boldsymbol{q}} + \dot{\boldsymbol{J}}(\boldsymbol{q})\dot{\boldsymbol{q}},\\
&\boldsymbol{\Lambda}(\boldsymbol{x}) = \boldsymbol{J}(\boldsymbol{q})^{-\mathrm{T}}\boldsymbol{H}(\boldsymbol{q})\boldsymbol{J}(\boldsymbol{q})^{-1},\\
&\boldsymbol{D}(\boldsymbol{x},\dot{\boldsymbol{x}}) = \boldsymbol{J}(\boldsymbol{q})^{-\mathrm{T}}\left(\boldsymbol{C}(\boldsymbol{q},\dot{\boldsymbol{q}}) - \boldsymbol{H}(\boldsymbol{q})\boldsymbol{J}(\boldsymbol{q})^{-1}\dot{\boldsymbol{J}}(\boldsymbol{q})\right)\boldsymbol{J}(\boldsymbol{q})^{-1},\\
&\boldsymbol{F}_g(\boldsymbol{x}) = \boldsymbol{J}(\boldsymbol{q})^{-\mathrm{T}}\boldsymbol{g}(\boldsymbol{q}),\\
&\boldsymbol{F}_\tau = \boldsymbol{J}(\boldsymbol{q})^{-\mathrm{T}}\boldsymbol{\tau},
\end{aligned}$$

and $\boldsymbol{\Lambda}(\boldsymbol{x}) \in \mathbb{R}^{6\times6}$ represents the Cartesian inertia matrix; $\boldsymbol{D}(\boldsymbol{x},\dot{\boldsymbol{x}}) \in \mathbb{R}^{6\times6}$ represents the Cartesian Coriolis and centrifugal matrix; $\boldsymbol{F}_g(\boldsymbol{x}) \in \mathbb{R}^6$ represents the Cartesian gravity force; and $\boldsymbol{F}_\tau \in \mathbb{R}^6$ represents the Cartesian driving force.

For the admittance control, the target admittance function of the Cartesian translation motion is formulated as

$$\boldsymbol{M}_p\ddot{\boldsymbol{e}}_p + \boldsymbol{B}_p\dot{\boldsymbol{e}}_p + \boldsymbol{K}_p\boldsymbol{e}_p = -\boldsymbol{F}_p, \tag{4}$$

where $\boldsymbol{M}_p, \boldsymbol{B}_p$, and $\boldsymbol{K}_p \in \mathbb{R}^{3\times3}$ are the corresponding translation mass, damping, and stiffness matrices, respectively; usually these three parameters are chosen as constant diagonal matrices for the decoupling effect [37]; and $\boldsymbol{e}_p = \boldsymbol{x}_p^d - \boldsymbol{x}_p^c \in \mathbb{R}^3$ represents the position trajectory modification, in which $\boldsymbol{x}_p^d \in \mathbb{R}^3$ represents the desired endpoint position input and $\boldsymbol{x}_p^c \in \mathbb{R}^3$ represents the compliant endpoint position output. As each Cartesian variable is independent in eq. (4), we focus on the one-dimensional translation case. Then, eq. (4) can be reduced into

$$M_p\ddot{e}_p + B_p\dot{e}_p + K_pe_p = -F_p. \tag{5}$$

Most industrial robots have excellent positioning accuracy under their position controllers, and these controllers yield sufficiently accurate path tracking, namely, $x_p \approx x_p^c$ [38]. When the admittance-based control system reaches the steady state, namely, $\ddot{e}_p = 0$ and $\dot{e}_p = 0$, we can reduce eq. (5) into the following expression:

$$K_p\left(x_p^d - x_p\right) = -F_p. \tag{6}$$

According to the relationship between the active endpoint force and the environmental reaction force, the linear environment model is considered in this paper. Without loss of generality, the one-dimensional translation case of the environment model can be regarded as a linear spring model with stiffness k_e and we can deduce the environmental reaction force as

$$F_p - F_{ip} = k_e\left(x_p^e - x_p\right), \tag{7}$$

where x_p^e is the environment position and F_{ip} represents the reaction force when the end-effector first contacts the environment. In general, the value of F_{ip} is approximately equal to 0, namely, $F_{ip} \approx 0$, so we can deduce

$$F_p = k_e\left(x_p^e - x_p\right). \tag{8}$$

By force feedback, the admittance controller regulates the contact force by modifying the end-effector position trajectory, which is suitable for position/velocity-controlled robots. Moreover, combining eqs. (6) and (8), we can obtain the endpoint force at the steady state as

$$F_p = \frac{K_pk_e\left(x_p^e - x_p^d\right)}{K_p + k_e}. \tag{9}$$

As we see, in eq. (9), both k_e and x_p^e are environmental parameters instead of control parameters. Thus, we can adjust x_p^d or K_p to regulate F_p.

2.2 Two typical force regulation strategies

According to the above analysis, there are two main strategies to regulate the endpoint force F_p: (1) modifying the endpoint position trajectory x_p^d and (2) adjusting the target impedance/admittance parameters. For the second method, designing online variable target stiffness K_v can regulate the interaction force.

(1) Environmental stiffness estimation (ESE)

An intuitive approach is given in ref. [15], in which the desired time-varying $x_p^d(t)$ is designed by estimating the environmental stiffness at a given time t, and constant mass, damping, and stiffness parameters are adopted in the target admittance function. For an unknown environment, its stiffness can be estimated by

$$\hat{k}_e = \frac{F_p}{x_p^e - x_p}. \tag{10}$$

Moreover, the composite stiffness is defined as

$$K_{ef} = \frac{K_pk_e}{K_p + k_e}. \tag{11}$$

If we want to obtain the desired endpoint force F_d, we can design a suitable desired trajectory according to eq. (9) as

$$\hat{x}_p^d = x_p^e - \frac{F_d}{\hat{K}_{ef}}, \tag{12}$$

where $\hat{K}_{ef} = \frac{K_p \hat{k}_e}{K_p + \hat{k}_e}$.

Remark 1: When the environmental stiffness is estimated, the desired trajectory $\hat{x}_p^d(t)$ can be obtained according to eq. (12). Meanwhile, $\dot{\hat{x}}_p^d(t)$ and $\ddot{\hat{x}}_p^d(t)$ are available.

The ESE admittance control algorithm can generate the following compliant trajectories:

$$\begin{cases} \ddot{x}_p^c(t) = \frac{F_p + B_p\left(\dot{\hat{x}}_p^d(t) - \dot{x}_p(t)\right) + K_p\left(\hat{x}_p^d(t) - x_p(t)\right)}{M_p} + \ddot{\hat{x}}_p^d(t), \\ \dot{x}_p^c(t+1) = \dot{x}_p(t) + \ddot{x}_p^c(t)\Delta t, \end{cases} \tag{13}$$

where x_p^c is the planned compliant trajectory; x_p is the real end-point position; and Δt is the sampling period.

(2) Variable target stiffness (VTS)

An admittance controller with variable target stiffness is proposed in ref. [20]. In Figure 3, the corresponding variable admittance function is written as

$$M_p\ddot{e}_p + B_p\dot{e}_p + K_v e_p = -F_p, \tag{14}$$

where K_v is the time-varying target stiffness coefficient. Meanwhile, the force error e_f is defined as

$$e_f = -F_d - \left(-F_p\right) = F_p - F_d. \tag{15}$$

The control law of K_v is designed as

$$K_v = \frac{k_p e_f + k_d \dot{e}_f}{e_p}, \tag{16}$$

where k_p and k_d are constant proportional and differential gains, respectively. $e_p = x_p^d - x_p^c$ is the deviation between the desired position and the planned compliant position. Note that the desired position is an arbitrary position set by users, and usually x_p^d is set to make e_p in eq. (16) never be 0.

As we see, K_v is determined by the force error and the position error in a PD manner. Substituting eq. (14) into eq. (15), we can obtain the closed-loop system as

$$e_f = -M_p\ddot{e}_p - B_p\dot{e}_p - K_v e_p - F_d. \tag{17}$$

Remark 2: For tracking a fixed position/trajectory x_p^d, the corresponding acceleration and velocity are $\dot{x}_p^d = \ddot{x}_p^d = 0$.

Combining eqs. (16) and (17), we can obtain the following control law:

$$\left(k_p + 1\right)e_f + k_d\dot{e}_f = -F_d + M_p\ddot{x}_p^c + B_p\dot{x}_p^c. \tag{18}$$

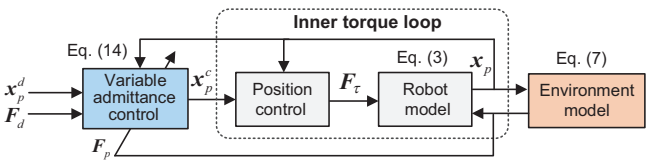

Figure 3 (Color online) Variable admittance control strategy.

The VTS control algorithm can generate the following compliant trajectories:

$$\begin{cases} \ddot{x}_p^c(t) = \dfrac{\left(k_p + 1\right)e_f(t) + k_d\dot{e}_f(t) + F_d(t) - B_p\dot{x}_p^c(t)}{M_p}, \\ \dot{x}_p^c(t+1) = \dot{x}_p(t) + \ddot{x}_p^c(t)\Delta t. \end{cases} \tag{19}$$

For the above admittance control with VTS, the corresponding stability analysis can be found in ref. [20]. However, the main drawback of the VTS strategy is its nonzero force-tracking performance in the steady phase.

As we see in eq. (9), the desired trajectory takes the numerator position, which may lead to a large force fluctuation due to a small estimation error of $\hat{x}_p^d$. In contrast, the target stiffness K_p behaves as a harmonious term, which leads to a gentle force fluctuation even with the calculation error of K_v. Meanwhile, as we see in eqs. (13) and (19), both admittance-based controllers need two-step calculations to determine the compliant end-effector velocity trajectory, namely, the first step calculates the acceleration trajectory, and the second step calculates the velocity trajectory.

3 Novel variable admittance controllers

For industrial low-bandwidth robots, complex control algorithms may weaken their control performance. Our purpose is to design effective and easy-to-use compliant controllers with adaptive force-tracking performance. Inspired by human arm stiffness adaptation behavior and VTS [20], we design a novel variable target stiffness (NVTS) controller and its enhancement. The stability and force-tracking capability of the proposed controllers are analyzed theoretically.

3.1 NVTS controller and its enhancement

According to eqs. (13) and (19), both equations need two steps to calculate the compliant velocity trajectory $\dot{x}_p^c(t)$. Since we want to design an efficient compliant control algorithm, we modify the target admittance function (14) by omitting the target mass term to obtain the first-order admittance model:

$$B_p\dot{e}_p + K_{Nv}e_p = -F_p, \tag{20}$$

where K_{Nv} is the NVTS coefficient. Combining eqs. (15) and (20), we can obtain the following closed-loop system:

$$e_f = -B_p\dot{e}_p - K_{Nv}e_p - F_d. \tag{21}$$

The control law of K_{Nv} is designed as

$$K_{Nv} = \frac{k_p e_f + k_i\int_0^t e_f dt + k_d\dot{e}_f}{e_p}, \tag{22}$$

where k_i is the integral gain and K_{Nv} is constructed by the force error and the position error in a PID-like manner [39]. Substituting eq. (22) into eq. (21), we can obtain the following closed-loop control system:

$$\left(k_p+1\right)e_f+k_i\int_0^t e_f\mathrm{d}t+k_d\dot{e}_f=-F_d-B_p\dot{e}_p. \tag{23}$$

According to Remark 2, the NVTS admittance control law can generate the following compliant trajectory:

$$\dot{x}_p^c(t)=\frac{\left(k_p+1\right)e_f(t)+k_i\int_0^t e_f(t)\,dt+k_d\dot{e}_f(t)+F_d(t)}{B_p}. \tag{24}$$

To facilitate the stability analysis of the NVTS controller, we introduce an intermediate variable

$$\begin{aligned}v_f(t)&=\dot{x}_p^c(t)B_p-F_d(t)\\&=\left(k_p+1\right)e_f(t)+k_i\int_0^t e_f(t)\,\mathrm{d}t+k_d\dot{e}_f(t),\end{aligned} \tag{25}$$

where $v_f(t)$ will be used in the stability analysis.

In addition, when the robot polishes machined parts its end-effector may be subjected to strong disturbances. As an enhancement, a simple impact compensator (Impc) is designed to be integrated into the NVST controller, which replaces the fixed damping coefficient B_p of eq. (24) with a variable damping coefficient $B(t)$ to attenuate the external interference. In the enhanced NVTS controller, the PID variable stiffness is still responsible for the force tracking, while the Impc is responsible for suppressing disturbances by evaluating the impact in a short time. As $B(t)$ is a bounded positive function, the stability of the enhanced NVTS controller remains the same as that of the NVTS controller. The detailed damping law of the Impc $B(t)$ is provided in the Appendix.

3.2 Stability and force-tracking capability

To analyze the stability and force-tracking property of the proposed controllers, some assumptions based on the classical control theory [40] are given as follows.

(1) For the position/velocity-controlled robot, the input and output are small Cartesian displacements, and the position controller of the robot can guarantee the accuracy of the end-effector. Its one-dimensional translation motion can be approximated by the first-order system [41] with time constant T_R. The corresponding transfer function is formulated as

$$G_R(s)=\frac{1}{1+T_Rs}, \tag{26}$$

where s is the Laplace variable.

(2) To simplify the Laplace transform, the initial environment location is defined as $x_p^e=0$.

(3) The desired force signal is considered to be a step-function signal with an amplitude of F_d.

Furthermore, we establish the control block diagram of the robot-environment interaction under the NVTS control strategy (Figure 4). According to eqs. (8), (15), and (24)–(26), some related equations are deduced as follows:

$$\begin{cases}E_f(s)=F_p(s)-F_d(s),\\V_f(s)=E_f(s)G_1(s),\\X_p^c(s)=\dfrac{V_f(s)+F_d(s)}{B_ps},\\X_p(s)=X_p^c(s)G_R(s),\\-F_p(s)=H_E(s)X_p(s),\end{cases} \tag{27}$$

where $E_f(s), F_p(s), F_d(s), V_f(s), X_p^c(s)$, and $X_p(s)$ are the Laplace transforms of $e_f, F_p, F_d, v_f, x_p^c$, and x_p, respectively; $G_1(s)$ is the transfer function of the intermediate variable; and $H_E(s)$ is the transfer function of the environment model. Note that the negative sign for the input $-F_d(s)$ and the output $-F_p(s)$ only indicates their direction.

According to eq. (25), the corresponding transfer function in the frequency domain can be written as

$$\begin{aligned}G_1(s)&=\frac{V_f(s)}{E_f(s)}=\left(k_p+1\right)+\frac{k_i}{s}+k_ds\\&=\frac{k_ds^2+\left(k_p+1\right)s+k_i}{s}.\end{aligned} \tag{28}$$

The closed-loop output $-F_p(s)$ is expressed as

$$-F_p(s)=\frac{\left(G_1(s)-1\right)G_R(s)H_E(s)}{G_1(s)G_R(s)H_E(s)+B_ps}\left(-F_d(s)\right), \tag{29}$$

where $H_E(s)=k_e$. The transfer function of the closed-loop system is deduced as

$$\begin{aligned}\Phi(s)&=\frac{-F_p(s)}{-F_d(s)}\\&=\frac{k_dk_es^2+k_pk_es+k_ik_e}{B_pT_Rs^3+\left(B_p+k_dk_e\right)s^2+\left(1+k_p\right)k_es+k_ik_e}.\end{aligned} \tag{30}$$

The characteristic equation of the closed-loop system is obtained as

$$D(s)=B_pT_Rs^3+\left(B_p+k_dk_e\right)s^2+\left(1+k_p\right)k_es+k_ik_e. \tag{31}$$

We can analyze the stability according to the Routh stability criterion [40]. The corresponding Routh-Hurwitz array can be obtained as

$$\begin{array}{lcc}s^3 & B_pT_R & \left(1+k_p\right)k_e\\ s^2 & B_p+k_dk_e & k_ik_e\\ s^1 & \frac{\left(\left(B_p+k_dk_e\right)\left(1+k_p\right)-B_pT_Rk_i\right)k_e}{B_p+k_dk_e} & 0\\ s^0 & k_ik_e & 0\end{array}.$$

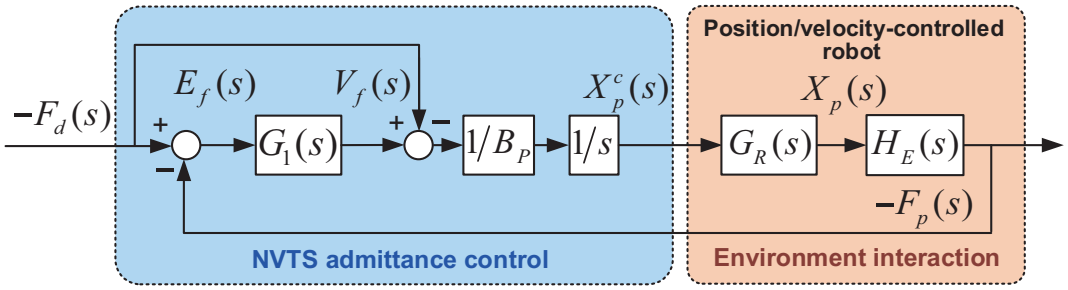

Figure 4 (Color online) Control block diagram of the system.

If each element of the first column in the Routh-Hurwitz array is larger than zero, the system is stable. In general, the environmental stiffness is $k_e > 0$ if we select $B_p > 0$, $k_p > 0$, $1 > k_i > 0$, and $k_d > 0$, and we can easily deduce $B_pT_R > 0$, $B_p + k_dk_e > 0$, and $k_ik_e > 0$. For the position/velocity-controlled robot system, T_R is the time constant that represents the system response speed, and usually T_R meets $1 > T_R > 0$. Moreover, we have $T_Rk_i \leqslant 1$, and we can deduce $\frac{((B_p+k_dk_e)(1+k_p)-B_pT_Rk_i)k_e}{B_p+k_dk_e} > 0$. Thus, the stability of the system is proven.

The force-tracking capability can be analyzed through the steady-state error, where the force error is expressed as

$$E_f(s) = \frac{B_ps + G_R(s)H_E(s)}{G_1(s)G_R(s)H_E(s) + B_ps}(-F_d(s)). \tag{32}$$

Substituting eqs. (26) and (28) into eq. (32), we can obtain

$$E_f(s) = \frac{\left(B_pT_Rs^3 + B_ps^2 + k_es\right)(-F_d(s))}{B_pT_Rs^3 + \left(B_p + k_dk_e\right)s^2 + \left(1 + k_p\right)k_es + k_ik_e}, \tag{33}$$

where $-F_d(s) = -\frac{F_d}{s}$ is the step input. According to the final value theorem of the Laplace transform, the steady-state error can be calculated as $e_{fss} = \lim_{s\to 0} sE_f(s) = 0$. Thus, the force-tracking property of the proposed controller is proven theoretically. Note that the above analyses also hold for the enhanced NVTS controller. Next, we will verify the proposed controller through various experiments.

4 Experimental studies

In this section, we carry out four groups of tests with different experimental settings (as listed in Table 1) to evaluate the effectiveness of the proposed NVTS controller. As we stated earlier, we aim to design a practical force-tracking controller for inexpensive position/velocity-controlled robots in unknown environments. Two different industrial manipulators are used: (1) the UR5 manipulator (from Universal Robots) with a low-bandwidth force/torque sensor (the sampling period t_p is 50 ms) and (2) the Xmate7Pro manipulator (from ROKAE) with a high-bandwidth force/torque sensor (the sampling period t_p is 4 ms). The first group is set up to compare the control performance of the NVTS method with the ESE and VTS methods in three touching tests with different environmental stiffness. The second group is set up to test the adaptability of the NVTS controller in different environmental geometries. The third group is set up to test the overshooting issue and the adaptability of the NVTS controller on different robots. In the first three groups, a passive cushion is installed at the endpoint of the manipulator for safety protection. The fourth group is set up to test the control performance of the NVTS controller when the robot is equipped with a polishing tool. Besides, the enhanced controller (namely, NVTS+Impc) will be tested to verify the extensibility of the NVTS control strategy. The parameters of the employed controllers are listed in Table 2, where mass and damping coefficients are set relatively high by the trial and error method to ensure that the end-effector approaching velocity is not too high [42]. Since we change the robot hardware, the parameters of the NVTS controller in Group 3 should be changed accordingly. For the enhanced controller the NVTS part is not changed, so only the control parameters of the Impc part are listed, which are defined in the Appendix. Moreover, two quantitative indices are used to analyze the results, namely, the mean contact force $\bar{F}_p$ and the corresponding standard deviation s_p in the steady phase.

$$\bar{F}_p = \frac{\sum_{i=1}^{n} F_p(i)}{n},\ s_p = \sqrt{\frac{\sum_{i=1}^{n}\left(F_p(i) - \bar{F}_p\right)^2}{n-1}}, \tag{34}$$

where $F_p(i)$ represents the contact force at the ith sampling time and n represents the total number of sampling times. $\bar{F}_p$ reflects the accuracy of force tracking and s_p reflects the stability of force tracking.

4.1 Group 1: Interaction with different environmental stiffness

As shown in Figure 5, we conduct three case studies in which three different materials (the sponge pad, the foam board, and the hard leather) are used to test the control performance of

Table 1 Experimental settings of test groups

Group	Robot	Method	Experimental condition
1	UR5	ESE [15] VTS [20] NVTS	Tests with different environmental stiffness
2	UR5	NVTS	Tests with different environmental geometries
3	Xmate7Pro	NVTS	Tests with different robots
4	Xmate7Pro	NVTS NVTS+Impc	Tests with a polishing tool

Table 2 Control parameters of controllers

Method	Robot	Control parameters
ESE	UR5	$M_p = 10000, B_p = 10000, K_p = 300, \hat{x}_p^d$ by eq. (12)
VTS	UR5	$k_p = 0.4, k_d = 5, M_p = 30000, B_p = 50000$
NVTS	UR5	$k_p = 0.4, k_i = 0.8, k_d = 5, B_p = 15000$
NVTS	Xmate7Pro	$k_p = 4, k_i = 0.00035, k_d = 0.1, B_p = 300$
NVTS+Impc	Xmate7Pro	$I_{S1} = 1.5, I_{S2} = 7.5, B_S = 100, B_C = 280$

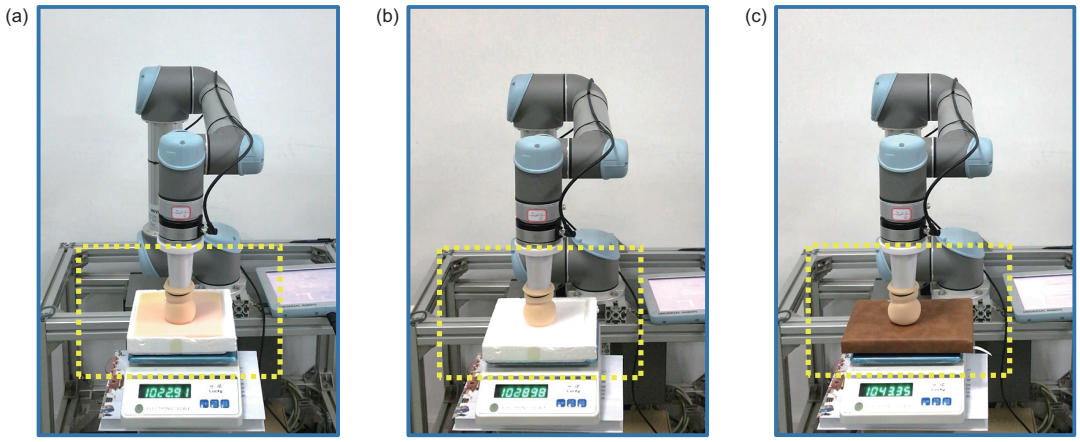

Figure 5 (Color online) Case studies on different environmental stiffness. (a) The sponge pad; (b) the foam board; (c) the hard leather.

the NVTS compared to the ESE and VTS methods. An electronic scale is used in this group to show the interaction force visually, which is helpful in tuning the control parameters. Similar setups can also be found in ref. [15].

The results of Group 1 are given in Figure 6. In Figure 6(a), for the ESE method, its contact force can basically guarantee the desired value with several small fluctuations; for the VTS method, its contact force is always higher than the desired value with a static error; for the NVTS method, its contact force almost remains at the desired value. In Figure 6(b), for the ESE method, its contact force is lower than the desired value with a small static error; for the VTS method, its contact force is higher than the desired value with many force fluctuations; for the NVTS method, its contact force is always stable around the desired value. In Figure 6(c), for the ESE method, its contact force is lower than the desired value with many large fluctuations; for the VTS method, its contact force is larger than the desired value with several fluctuations; for the NVTS method, after several small fluctuations in the initial phase, the contact force is stable around the desired value. The statistical analysis of each case ($t \geqslant 60$ s) is shown in Figure 6(d).

As we see, the ESE and VTS methods experience instability when the environmental stiffness increases. For the ESE method, the estimated trajectory takes the numerator position in eq. (9), so a small estimation error of $\hat{x}_p^d$ will lead to a large fluctuation. For the VTS method, the static force error cannot be neglected. The NVTS method shows the most accurate and stable performance among the three methods.

4.2 Group 2: Interaction with different environmental geometries

In Group 2, we further verify the control performance of the NVTS method on different environmental geometries. As shown in Figure 7, we aim to keep the end-effector tracking

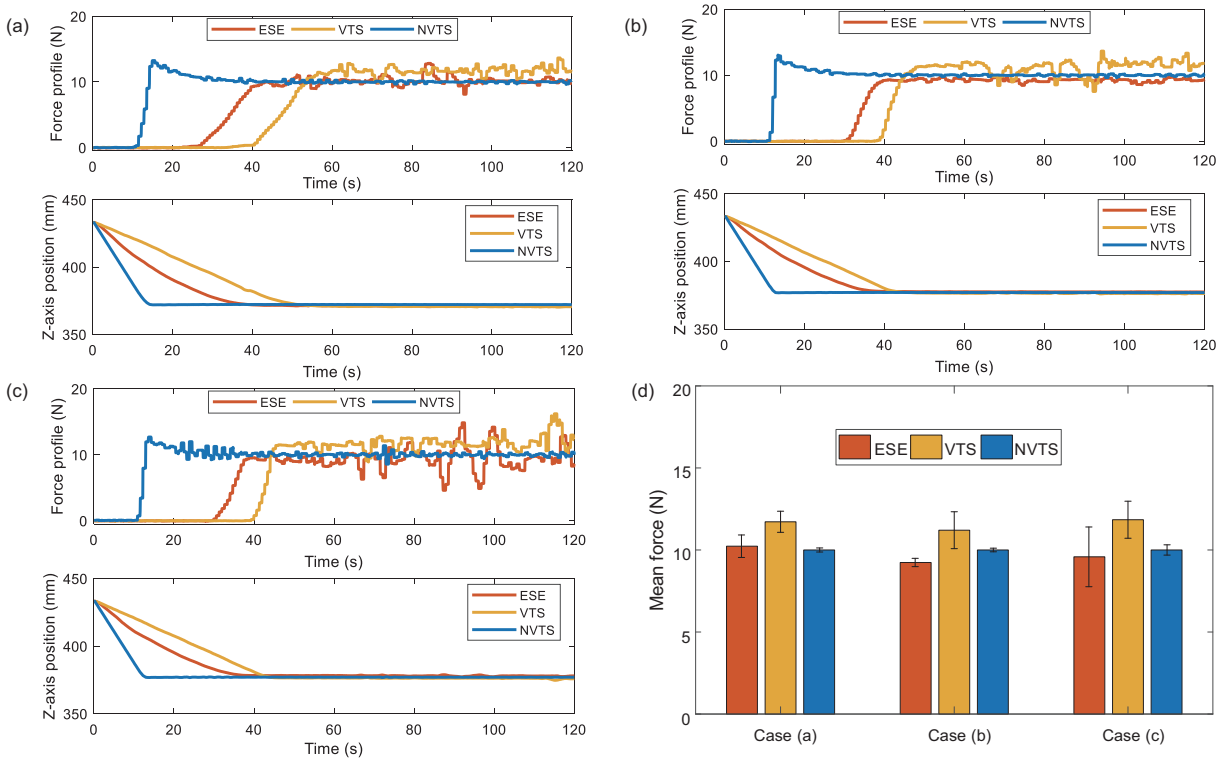

Figure 6 (Color online) Control results of Group 1. (a)–(c) The control performance on three different environmental stiffness; (d) force-tracking analyses of Group 1.

Figure 7 (Color online) Case studies on different environmental geometries: (a) the flat surface, (b) the slope surface, and (c) the curved surface.

on three geometrical environments (flat, slope, and curved surfaces) with a constant vertical force at a given horizontal velocity. In Figure 7(a) and (b), the shell of an iron box is selected as the interaction environment. In Figure 7(c), a curved surface made of engineering plastics is selected as the interaction environment. The desired force is set as F_d = 10 N, v_x = 5 mm/s is used in Figure 7(a) and (b), and a slow velocity v_x = 2 mm/s is used in Figure 7(c) due to the curvature

change on this surface.

The corresponding control results are given in Figure 8, and it is clear that the proposed controller can achieve stable and accurate force-tracking performance on three surfaces. The statistical analysis of each case ($t \geqslant 40$ s) is shown in Figure 8(d), where the mean force $\bar{F}_p$ is 10.04, 10.12, and 9.91 N, respectively, and the corresponding standard deviation s_p is 0.25, 0.26, and 0.35 N, respectively. Figure 8(a) has two force fluctuations because the shell of the iron box deforms randomly under concentrated force. However, obvious overshoots exist in the contact phase of each case and the corresponding maximum force F_{pmax} is 15.93, 14.76, and 14.07 N, respectively. The main reason for these overshoots is the large control interval of the robot system that limits the reaction speed of the robot system. It is difficult to avoid this phenomenon in hard environments for a robot with a low bandwidth sensor system.

4.3 Group 3: Interaction using different robot hardware

As overshoots occur on the UR5 robot with a low-bandwidth sensor, we further verify the control performance of the NVTS method on the Xmate7Pro robot (with a relatively high bandwidth sensor). The experimental settings of Group 3 remain the same as those of Group 2. The desired force is set as $F_d = 10$ N and $v_x = 6.5$ mm/s is implemented in each case. Likewise, we aim to control the end-effector to track three environments (Figure 9) with a constant vertical force. The corresponding control results are shown in Figure 10. When the Xmate7Pro robot is moving, the proposed controller can achieve stable and accurate force-tracking performance on different surfaces. Apparently, there are no overshoots in the contact phase of each case which verifies that the overshoots in Group 2 are mainly caused by the control frequency of the robotic hardware system.

Figure 10(a) and (b) show a few force fluctuations because of the deformation of the iron box. The statistical results ($(t \geqslant 40$ s)) in Figure 10(d) show that the maximum force F_{pmax} is 12.04, 11.30, and 11.62 N, respectively, which is not caused by the overshoot but by random disturbances from environments. Besides, the mean force $\bar{F}_p$ of each case is 9.99, 10.00, and 9.94 N and the corresponding standard deviation s_p is 0.45, 0.36, and 0.48 N, which illustrate that the NVTS method can achieve good adaptability on different robots.

4.4 Group 4: Interaction with a polishing tool

In Group 4, we installed a polishing tool at the end of the Xmate7Pro robot as shown in Figure 11. The experimental settings and the control parameters of the NVTS method remain the same as in Group 3. As the rotation of the polishing tool brings vibration to the endpoint, we aim to test the NVST controller under external disturbances. In practice, vibration disturbances may worsen the control performance of the

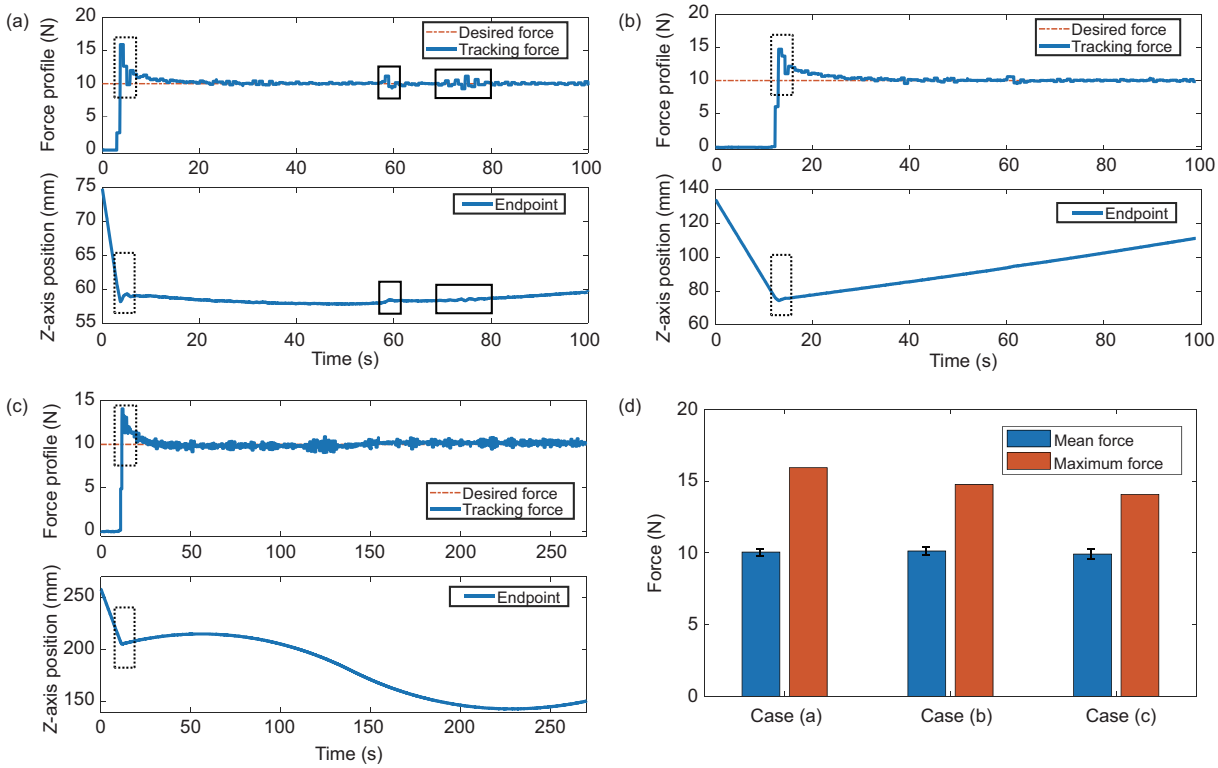

Figure 8 (Color online) Control results of Group 2. (a)–(c) The control performance on three different environmental geometries; (d) force-tracking analyses of Group 2.

Figure 9 (Color online) Case studies using a different robot: (a) the flat surface, (b) the slope surface, and (c) the curved surface.

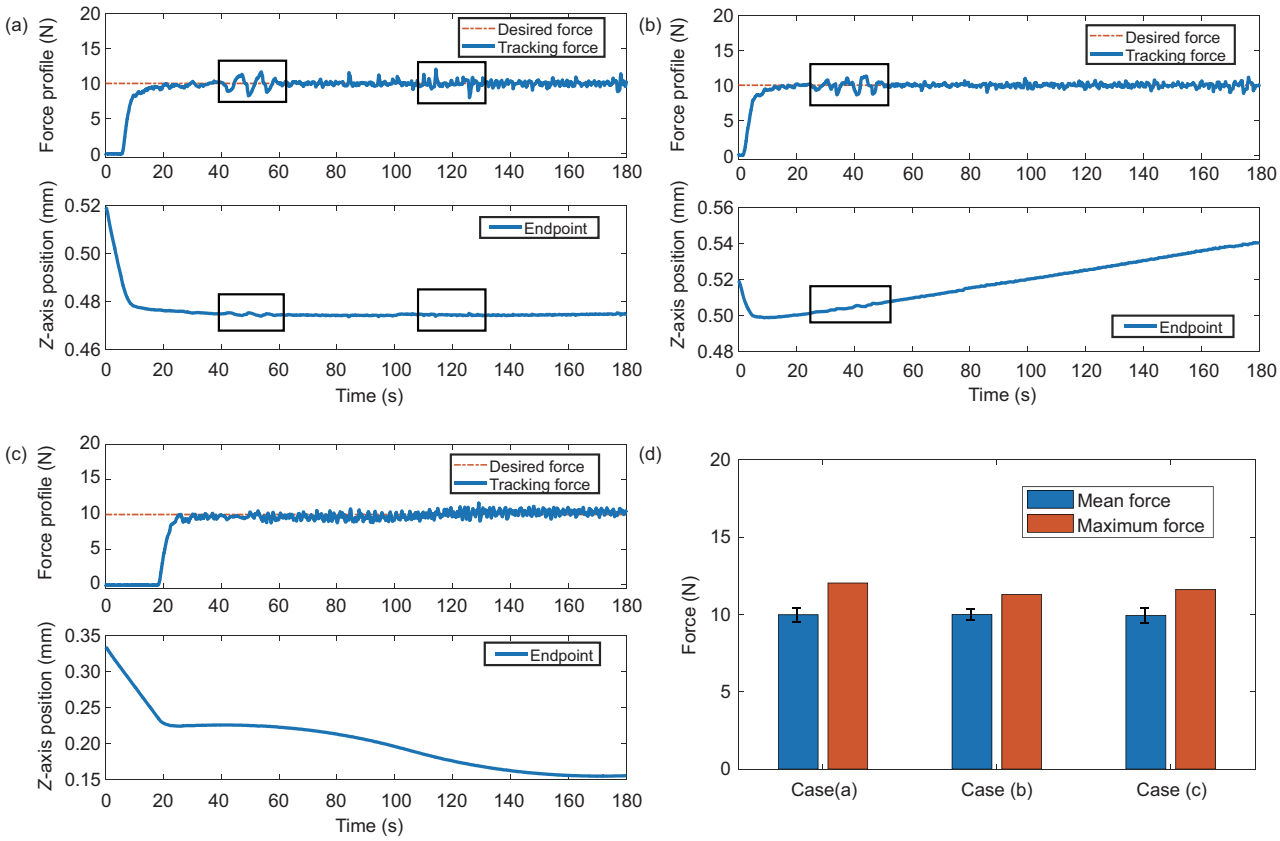

Figure 10 (Color online) Control results of Group 3. (a)–(c) The control performance on three different environmental geometries; (d) force-tracking analyses of Group 3.

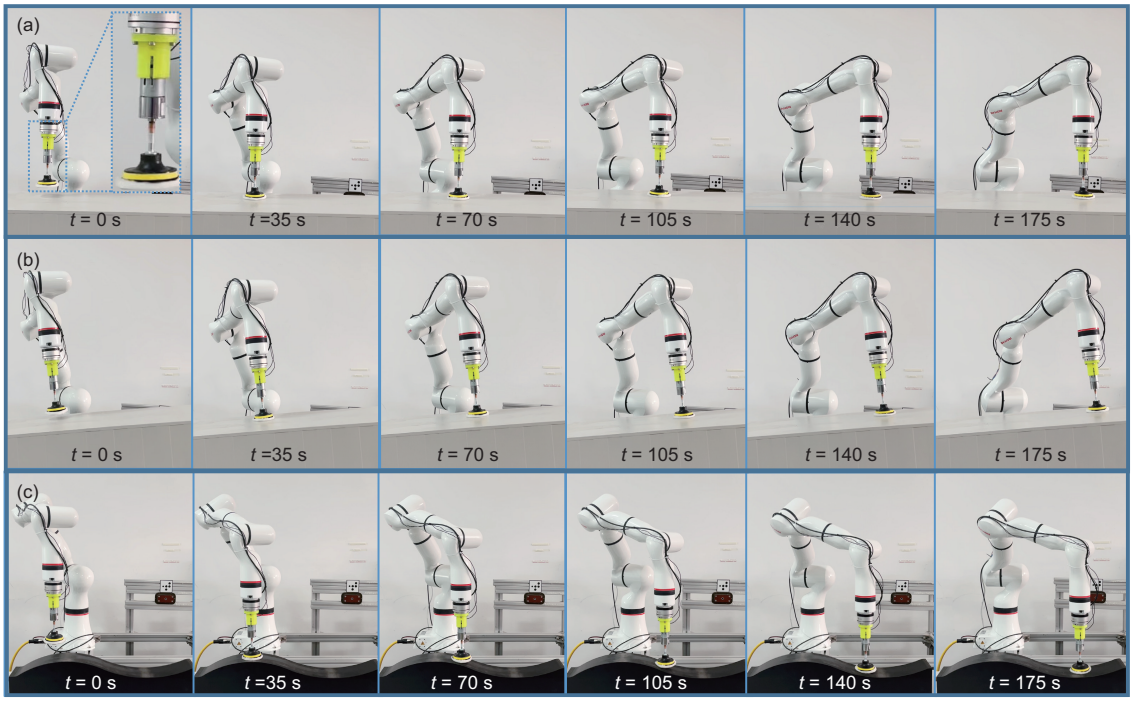

Figure 11 (Color online) Case studies with a polishing tool: (a) the flat surface, (b) the slope surface, and (c) the curved surface.

NVTS method. As external disturbances increase with the surface complexity, the enhanced NVTS controller (namely, NVTS+Impc) will be tested in Figure 11(c). The designed Impc regulates the damping coefficient of the NVTS controller by evaluating the short-time impact. When the vibration is strong that means the robot is subjected to violent impact, the impact function will get a high value and regulate the target damping coefficient to suppress disturbances.

For the enhanced controller, both stiffness and damping coefficients are updated in the target admittance function. The experimental results of the two controllers are shown in Figure 12. The statistical results of the two controllers (($t \geqslant 40$ s)) are shown in Figure 12(d). In Figure 12(a) and (b), the NVTS method and the enhanced NVTS method have similar control performances. In Figure 12(a), the mean force $\bar{F}_p$ of the NVTS and enhanced NVTS methods is 9.96 and 9.97 N, respectively; the corresponding standard deviation s_p is 0.58 and 0.47 N, respectively; and the corresponding maximum force F_{pmax} is 13.07 and 11.74 N, respectively. In Figure 12(b), the mean force $\bar{F}_p$ of the NVTS and enhanced NVTS methods is 10.04 and 10.06 N, respectively; the corresponding standard deviation s_p is 0.68 and 0.58 N, respectively; and the corresponding maximum force F_{pmax} is 12.38 and 12.67 N, respectively. In comparison, the enhanced NVTS method has better performance than the NVTS method in Figure 12(c). Herein, the mean force $\bar{F}_p$ of the NVTS and enhanced NVTS methods is 9.72 and 9.74 N, respectively; the corresponding standard deviation s_p is 1.90 and 1.37 N, respectively; and the corresponding maximum force F_{pmax} is 15.29 and 13.85 N, respectively.

4.5 Analysis and discussion

Compared with the ESE and VST methods, the NVST method has the advantages of computational simplicity and high accuracy. The detailed statistical results are listed in Table 3. In Group 1, it is obvious that the NVTS method achieves the most accurate tracking force and the minimum standard deviation among the three methods. Although some overshoots occur in the contact phase of Group 2, the main reason is due to the control interval of the robot system. Furthermore, vibration disturbances are considered in Group 4, where a polishing tool is installed at the end of the manipulator with some external disturbances. When the polished surface is not complicated, the NVTS method has satisfactory performance (see the results of Cases (a) and (b) in Group 4). When the external disturbance of Case (c) is strong, the Impc can reinforce the NVTS method with disturbance-suppression capabilities, where s_p decreases from 1.90 to 1.37 N. Meanwhile, it should be noted that the complexity of the enhanced controller has also increased accordingly because more parameters need to be determined.

5 Conclusion

This paper proposes an NVTS control strategy with its enhan-

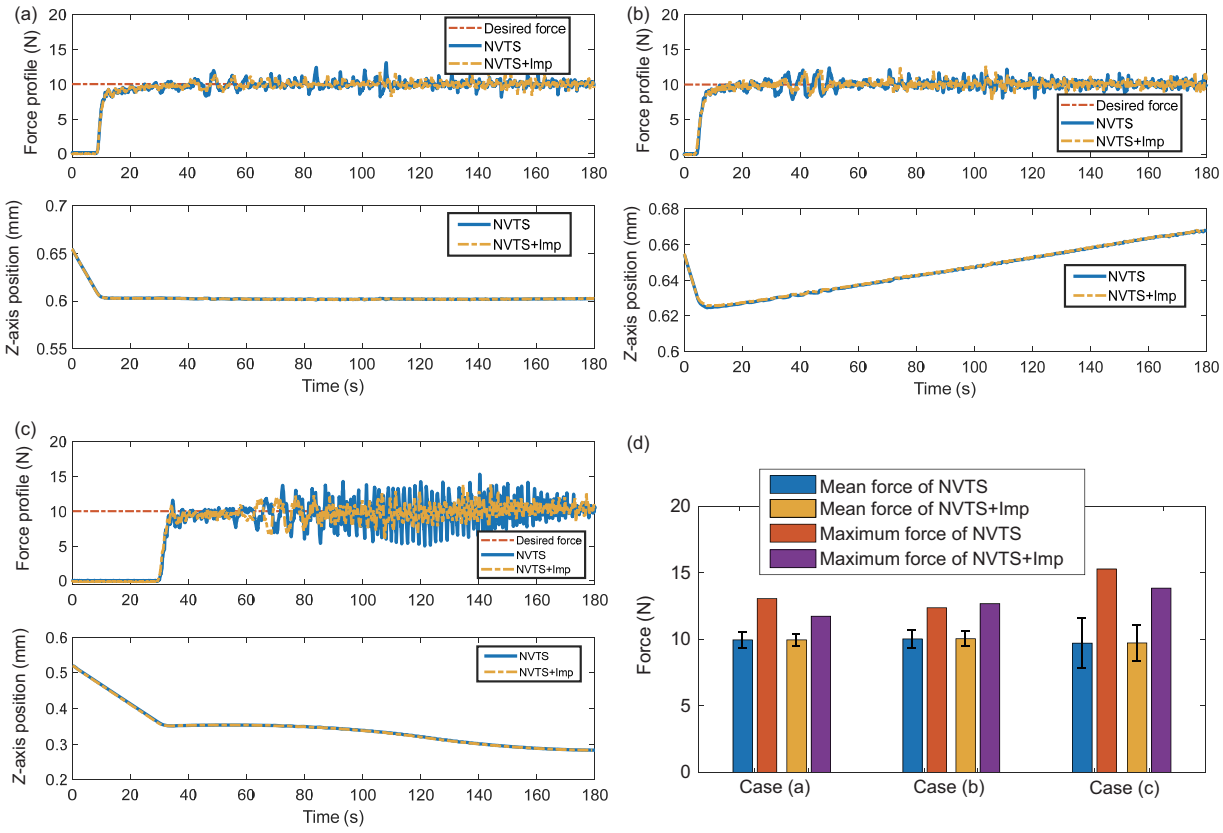

Figure 12 (Color online) Control results of Group 4. (a)–(c) The control performance on three different environmental geometries; (d) force-tracking analyses of Group 4.

Table 3 Statistical analyses of group studies

Group	Case	Robot	Method	$\bar{F}_p$ (N)	s_p (N)	F_{pmax} (N)
1	(a)	UR5	ESE	10.23	0.685	–
			VTS	11.72	0.643	–
			NVTS	**10.00**	**0.124**	–
	(b)		ESE	9.24	0.25	–
			VTS	11.20	1.12	–
			NVTS	**10.00**	**0.109**	–
	(c)		ESE	9.58	1.82	–
			VTS	11.85	1.128	–
			NVTS	**10.00**	**0.31**	–
2	(a)	**UR5**	NVTS	10.04	0.25	**15.93**
	(b)			10.12	0.26	**14.76**
	(c)			9.91	0.35	**14.07**
3	(a)	**Xmate7Pro**	NVTS	9.99	0.45	**12.04**
	(b)			10.00	0.36	**11.30**
	(c)			9.94	0.48	**11.62**
4	(a)	Xmate7Pro	NVTS	9.96	**0.58**	**13.07**
			NVTS+Impc	9.97	**0.47**	**11.74**
	(b)		NVTS	10.04	**0.68**	**12.38**
			NVTS+Impc	10.06	**0.58**	**12.67**
	(c)		NVTS	9.72	**1.90**	**15.29**
			NVTS+Impc	9.74	**1.37**	**13.85**

cement to achieve high-accuracy force tracking, in which a PID variable stiffness law is designed to update the stiffness coefficient. The proposed NVTS controller has strong practicality in various unknown force-tracking scenarios with several advantages such as (1) computational simplicity without estimating the environment model, (2) high-accuracy force tracking with zero steady-state error, (3) strong adaptability, and (4) extensibility. Four groups of experimental tests are conducted to validate the effectiveness of the proposed controllers. Comparative studies of Group 1 illustrate that the NVTS method can achieve the highest-accuracy force tracking with $\bar{F}_p = 10$ N among three admittance-based controllers. The results of Group 2 and Group 3 verify its adaptive force-tracking performance on different environmental geometries using two different robot hardware. The results of Group 4 illustrate that the NVTS method performs well under slight disturbances and its enhancement can reinforce the disturbance-suppression ability when external disturbances are strong.

Appendix

Following the modelling approach in ref. [43], a simple Impc is designed to regulate the damping coefficient of the NVTS controller (24). First, an impact function in a short time Δt is defined as

$$I^{Imp} = \int_{ts}^{ts+\Delta t} \left| \bar{F}_{ps} - F_d \right|, \tag{a1}$$

where $\Delta t = 10t_p$; t_p is the sampling period of the robot; and $\bar{F}_{ps} = \frac{\sum_{i=1}^{\Delta t/t_p} F_p(i)}{\Delta t/t_p}$ is the mean force during Δt. By evaluating eq. (a1), the variable damping coefficient of the Impc $B(t)$ is designed as

$$B(t) = \begin{cases} B_p, & I^{Imp} \leqslant I_{S1}, \\ \tanh(\chi)B_S + B_C, & I^{Imp} > I_{S1}, \end{cases} \tag{a2}$$

$$\chi = I^{Imp}/I_{S2},\ \tanh(\chi) = \frac{e^{\chi} - e^{-\chi}}{e^{\chi} + e^{-\chi}}, \tag{a3}$$

where B_S and B_C are damping parameters and I_{S1} and I_{S2} are impact evaluation parameters, which are obtained by the trial-and-error method. As we see $B(t)$ always meets $B(t) > 0$, the stability of the enhanced controller remains the same as the NVTS controller according to the stability analysis in Section 3.2.

This work was supported by the National Natural Science Foundation of China (Grant Nos. 62103407, 52075530, and 52175272), and the State Key Laboratory of Robotics Foundation (Grant No. Y91Z0303).

1 Villani L, De Schutter J. Force control. In: Springer Handbook of Robotics. Cham: Springer, 2016. 195–220
2 Bernier C. Polishing Robots: Automating the Finishing Process. 2022. https://howtorobot.com/expert-insight/polishing-robots
3 Chen H, Liu Y. Robotic assembly automation using robust compliant control. Robotics Comput-Integrated Manuf, 2013, 29: 293–300
4 Schumacher M, Wojtusch J, Beckerle P, et al. An introductory review of active compliant control. Robotics Autonomous Syst, 2019, 119: 185–200
5 Whitney D E. Force feedback control of manipulator fine motions. J Dyn Syst Measure Control, 1997, 99: 91–97
6 Raibert M H, Craig J J. Hybrid position/force control of manipulators. J Dyn Syst Measure Control, 1981, 103: 126–133
7 Chiaverini S, Sciavicco L. The parallel approach to force/position control of robotic manipulators. IEEE Trans Robot Automat, 1993, 9: 361–373
8 Karayiannidis Y, Rovithakis G, Doulgeri Z. Force/position tracking for a robotic manipulator in compliant contact with a surface using neuro-adaptive control. Automatica, 2007, 43: 1281–1288
9 Hogan N. Impedance control: An approach to manipulation: Part I-Theory. J Dyn Syst Measure Control, 1985, 107: 1–7
10 Ott C, Mukherjee R, Nakamura Y. Unified impedance and admittance control. In: Proceedings of the IEEE International Conference on Robotics and Automation. Anchorage, 2010. 554–561
11 Seul Jung , Hsia T C. Neural network impedance force control of robot manipulator. IEEE Trans Ind Electron, 1998, 45: 451–461
12 Valency T, Zacksenhouse M. Accuracy/robustness dilemma in impedance control. J Dyn Syst Measure Control, 2003, 125: 310–319
13 Natale C. Interaction Control of Robot Manipulators: Six Degrees-of Freedom Tasks. Vol. 3. Berlin, Heidelberg: Springer-Verlag, 2003
14 Duan J, Gan Y, Chen M, et al. Adaptive variable impedance control for dynamic contact force tracking in uncertain environment. Robotics Autonomous Syst, 2018, 102: 54–65
15 Jung S, Hsia T C, Bonitz R G. Force tracking impedance control for robot manipulators with an unknown environment: theory, simulation, and experiment. Int J Robotics Res, 2001, 20: 765–774
16 Zhang X, Liu J, Gao Q, et al. Adaptive robust decoupling control of multi-arm space robots using time-delay estimation technique. Nonlinear Dyn, 2020, 100: 2449–2467
17 Lee C H, Wang W C. Robust adaptive position and force controller design of robot manipulator using fuzzy neural networks. Nonlinear Dyn, 2016, 85: 343–354
18 Roveda L, Pedrocchi N, Tosatti L M. Exploiting impedance shaping approaches to overcome force overshoots in delicate interaction tasks. Int J Adv Robot Syst, 2016, 13: 1–11
19 Seraji H. Adaptive admittance control: An approach to explicit force control in compliant motion. In: Proceedings of the IEEE International Conference On Robotics And Automation. San Diego, 1994. 2705–2712
20 Lee K, Buss M. Force tracking impedance control with variable target stiffness. IFAC Proc Volumes, 2008, 41: 6751–6756
21 Roveda L, Castaman N, Franceschi P, et al. A control framework definition to overcome position/interaction dynamics uncertainties in force-controlled tasks. In: Proceedings of the IEEE International Conference on Robotics and Automation. Paris, 2020. 6819–6825
22 Balatti P, Kanoulas D, Tsagarakis N, et al. A method for autonomous robotic manipulation through exploratory interactions with uncertain environments. Auton Robot, 2020, 44: 1395–1410
23 Ferraguti F, Secchi C, Fantuzzi C. A tank-based approach to impedance control with variable stiffness. In: Proceedings of the IEEE International Conference On Robotics and Automation. Karlsruhe, 2013. 4948–4953
24 Ding L, Xing H, Gao H, et al. VDC-based admittance control of multi-DOF manipulators considering joint flexibility via hierarchical control framework. Control Eng Pract, 2022, 124: 105186
25 Peng G, Yang C, He W, et al. Force sensorless admittance control with neural learning for robots with actuator saturation. IEEE Trans Ind

Electron, 2019, 67: 3138–3148
26 He W, Xue C, Yu X, et al. Admittance-based controller design for physical human-robot interaction in the constrained task space. IEEE Trans Automat Sci Eng, 2020, 17: 1937–1949
27 Li Y, Ge S S. Impedance learning for robots interacting with unknown environments. IEEE Trans Contr Syst Technol, 2013, 22: 1422–1432
28 Hamedani M H, Sadeghian H, Zekri M, et al. Intelligent impedance control using wavelet neural network for dynamic contact force tracking in unknown varying environments. Control Eng Pract, 2021, 113: 104840
29 He W, Dong Y. Adaptive fuzzy neural network control for a constrained robot using impedance learning. IEEE Trans Neural Netw Learn Syst, 2017, 29: 1174–1186
30 Roveda L, Riva D, Bucca G, et al. Sensorless optimal switching impact/force controller. IEEE Access, 2021, 9: 158167
31 Roveda L, Veerappan P, Maccarini M, et al. A human-centric framework for robotic task learning and optimization. J Manuf Syst, 2023, 67: 68–79
32 Ajoudani A, Tsagarakis N, Bicchi A. Tele-impedance: Teleoperation with impedance regulation using a body-machine interface. Int J Robotics Res, 2012, 31: 1642–1656
33 Yang C, Ganesh G, Haddadin S, et al. Human-like adaptation of force and impedance in stable and unstable interactions. IEEE Trans Robot, 2011, 27: 918–930
34 Yang C, Zeng C, Fang C, et al. A DMPs-based framework for robot learning and generalization of humanlike variable impedance skills. IEEE ASME Trans Mechatron, 2018, 23: 1193–1203
35 Wu Y, Zhao F, Tao T, et al. A framework for autonomous impedance regulation of robots based on imitation learning and optimal control. IEEE Robot Autom Lett, 2020, 6: 127–134
36 Ott C. Cartesian Impedance Control of Redundant and Flexible-Joint Robots. Berlin, Heidelberg: Springer, 2008
37 Zhang X, Liu J, Tong Y, et al. Attitude decoupling control of semifloating space robots using time-delay estimation and supertwisting control. IEEE Trans Aerosp Electron Syst, 2021, 57: 4280–4295
38 Swevers J, Verdonck W, De Schutter J. Dynamic model identification for industrial robots. IEEE Control Syst Mag, 2007, 27: 58–71
39 Åström K J, Hägglund T. The future of PID control. Control Eng Pract, 2001, 9: 1163–1175
40 Katsuhiko O. Modern Control Engineering. Vol. 5. Upper Saddle River: Prentice Hall, 2010
41 Winkler A, Suchy J. Identification and controller design for the inverted pendulum actuated by a position controlled robot. In: Proceedings of the International Conference on Methods & Models in Automation & Robotics. Miedzyzdroje, 2013. 285–293
42 Kang G, Oh H S, Seo J K, et al. Variable admittance control of robot manipulators based on human intention. IEEE ASME Trans Mechatron, 2019, 24: 1023–1032
43 Roveda L, Iannacci N, Vicentini F, et al. Optimal impedance force-tracking control design with impact formulation for interaction tasks. IEEE Robot Autom Lett, 2015, 1: 130–136